Composites Part B 280 (2024) 111474

Contents lists available at ScienceDirect

Composites Part B

journal homepage: www.elsevier.com/locate/compositesb

Silk-inspired architectured filament with enhanced stiffness and toughness for Fused deposition modelling (FDM)

Li Liang [a], Filippo Berto [b], Chao Gao [a,*]

[a] Department of Mechanical and Industrial Engineering, Norwegian University of Science and Technology (NTNU), Richard Birkelands Vei 2b, 7491, Trondheim, Norway
[b] Department of Chemical Materials, Environmental Engineering, Sapienza University of Rome, Rome, 00185, Italy

ARTICLE INFO

Handling Editor: Prof. Ole Thomsen

Keywords:
Bio-inspired design
Mechanical properties
Architectured materials
Mechanical testing

ABSTRACT

Architectured materials, those capable of manipulating the spatial configurations of two or more material phases, have recently gained substantial attention, primarily due to their unprecedented material properties (e.g., exceptional strength-to-weight ratio and intriguing negative Poisson's ratio). Most architectured materials draw inspiration from the microstructure of natural solutions. One of fascinating examples are spider silk and cocoon silk. Their multimaterial core-shell fibrous structure exhibits remarkable mechanical properties—high stiffness, strength, and toughness. In this study, silk-inspired dual-phase Core-Shell Architectured Filament (CSAF), which combines a rigid Polylactic Acid (PLA) core with a soft Thermoplastic Polyurethane (TPU) shell, was developed as feedstock for additive manufacturing. The mechanical testing of dual-phase CASF printed samples reveal intriguing results. Notably, the optimized CASF in this study, whose volume fraction of rigid core was set as 52 %, was observed a substantial improvement of the printed specimens in initial stiffness and energy absorption capacity—up to a remarkable 14-fold increase in initial stiffness and a ~9 % enhancement in energy absorption when compared to the pure TPU filament. To gain a deeper understanding of the synergistic effects arising from geometrical and material configurations on the structure's damage mechanism, a theoretical model of this core-shell structure was developed. Computational models have been built to validate theoretical model, and the results from finite element analysis are in excellent agreement with experimental results. These discoveries offer valuable insights to enhance mechanical performance of the feedstock for additive manufacturing.

1. Introduction

Demand for high-performance materials—e.g., lightweight, high stiffness, strength and energy absorption—increases significantly in modern industrial applications, and traditional monolithic materials have challenges to meet the demand because of their intrinsic properties. Hybrid materials, which combine two or more materials with distinct properties and complementary each other, have been developed to tackle challenges from industry for decades [1]. Recently, architectured materials make its way into the mainstream of hybrid material design. Unlike traditional chemical-based and micromechanics-based approaches, the design of architectured materials focuses on mesostructural layout—a length scale between the microstructural scale and the macroscopic scale of the specimen dimensions [2]. By rationally designing mesostructural layout of architectured materials, researchers have successfully developed high-performance materials such as cellular materials, lattice materials and multilayered materials [3,4]. However, designing new architectured materials with remarkable properties is still challenging because of two reasons—(i) there is no certain principles for material selection and the design of mesostructural layout; and (ii) the fabrication of architectured materials with multiple material phases and complicated structure is still difficult.

One of the promising approaches to design new architectured materials is bio-inspired design because many living organisms have evolved materials with extraordinary properties over billions of years evolution [5]. For example, many biological materials—e.g., nacre [6,7], beetle forewings [8–10] and bone [11,12]—achieve superior mechanical performance by employing very few poor-performance base materials. By extracting design principles from these biological materials, bio-inspired architectured materials have been designed successfully to achieve unprecedented properties [13–15]. Furthermore, multimaterial additive manufacturing technologies make it an ideal approach to the fabrication of bio-inspired architectured materials [16–28]. For instance, Sun et al. [18] fabricated carefully designed

* Corresponding author.
E-mail address: chao.gao@ntnu.no (C. Gao).

https://doi.org/10.1016/j.compositesb.2024.111474
Received 14 November 2023; Received in revised form 8 April 2024; Accepted 16 April 2024
Available online 18 April 2024

twisted plywood structure, which is also known as Bouligand structure, inspired by the shell of *Homarus americanus* (American lobster) via Fused deposition modelling (FDM) technology. The bio-inspired design has significantly increased the fracture deflection and energy absorption of FDM printed parts by numerical and experimental optimization of the rotational angle of twisted layers. Another excellent example is FDM printed nacre-inspired design by employing stiff polylactic acid (PLA) and soft thermoplastic polyurethane (TPU) [24]. The remarkable improvement in the energy absorption of nacre-inspired design has been verified by experimental study. These examples clearly demonstrate the great potential of bio-inspired architectured materials fabricated by multimaterial additive manufacturing technology.

More recently, many multimaterial biological fibrous materials have increasingly received attention from scientists and engineers due to their notable mechanical properties and versatile functions. For instance, spider silk, whose function is to construct web, capture and cocoon prey, has been characterized by its excellent performance in strength and toughness [29–31]. The core-shell mesostructural layout of spider silk fiber—stiff crystalline core embedded in soft amorphous shell, as shown in Fig. 1a—has been identified as one of the critical contributions to enhance mechanical properties of spider silk [32–34]. As another typical example, cocoon silk from silkworms, which has been one of the oldest commercial products in textile industry [35], has also shown remarkable mechanical behaviors by employing core-shell design [36–38] (Fig. 1b and c).

In this paper, multimaterial core-shell design inspired by these natural fibrous structures is proposed to be employed as the inner structure of FDM filament. This dual-phase Core-Shell Architectured Filament (CSAF) employs stiff material surrounded by soft material. The dual-phase CSAFs were fabricated directly by FDM process and loaded in a commercial FDM 3D printer to print high quality multi-material parts without additional hardware upgrades. To study the mechanical performance of printed parts using the dual-phase CSAF, uniaxial tensile tests were conducted at quasi-static condition. Deformation and damage mechanism were analyzed analytically and numerically. A comprehensive comparison of results from theoretical models, numerical simulations, and experimental testing was provided. Further, the prediction of mechanical properties as a function of material combinations and the limitation of materials selection were discussed through the theoretical model. Interestingly, the results show that bio-inspired filament behaves much stiffer and tougher than its base materials. Furthermore, the wide choice of core and shell materials offers the potential for various functionalities, including moisture resistance, oxidation resistance, UV resistance, wear resistance, electrical conductivity, and lubrication.

2. Methods

2.1. Materials

The core material used in this study was Prusament PLA Jet Black produced by Prusa Research. It is known for its high stiffness, high strength but brittle nature. The shell material employed was 3DNet TPU Transparent purchased from 3DNet. This material features softness and high elongation. It is a hyperelastic material that is easy to deform at the beginning but can hold high load at heavy stretching. A water-soluble support material, 3ntr SSU04, manufactured by 3ntr company, was used to provide support during the printing process, specifically for bridges or overhang structures.

2.2. Preparation of dual-phase CSAF

There are various approaches to manufacture composite filaments for FDM printing, such as, vacuum infusion, compression moulding, injection moulding, direct extrusion, co-extrusion with towpreg, inline impregnation, in-situ impregnation, additive manufacturing and other techniques [39–48]. In this research, based on the laboratory capacity, additive manufacturing was selected to produce the dual-phase CSAFs. A triple-nozzle FDM printer, 3ntr A4v4, was utilized to fabricate dual-phase CSAFs at millimeter scale. To ensure consistent manufacturing quality, printing parameters—e.g., printing speed, retraction, temperature—were carefully controlled and optimized by performing parametrical study. The identified optimal parameters were then applied in the production of the dual-phase CSAFs, as shown in Table 1. Three different volume fractions (14 %, 34 %, and 52 %) of core material of the dual-phase CSAFs—noted as CSAF-PLA14 %, CSAF-PLA34 %, and CSAF-PLA52%—were fabricated and prepared for the production of dogbone specimen. Fig. 2 (a) demonstrates the fabrication process of CSAFs, accompanied by an optical microscopy image illustrating the cross-section of CSAF-PLA34 %.

2.3. Preparation of samples

To study the mechanical performance of printed part using the dual-phase CSAF, standard samples for uniaxial tension test have been fabricated by 3ntr A4v4 FDM printer. Because the printing process involves the extrusion of two different materials though a single nozzle, the potential blending issues need to be considered. Here we introduce Reynolds number, R, which is used to classify the flow types into laminar flow, critical flow, and turbulent flow. R is calculated as follows [49].

Table 1
The printing parameters for printing dual-phase CSAFs.

Materials	SSU04	PLA	TPU
Filament diameter (mm)	2.85	1.75	2.85
Nozzle diameter (mm)	0.4	0.3	0.3
Extrusion width (mm)	0.6	0.3	0.3
1st layer thickness (mm)	0.6	0.1	0.1
Layer thickness (mm)	0.15	0.1	0.1
Heat bed temperature (°C)	60	60	60
Chamber temperature (°C)	30	30	30
Nozzle temperature (°C)	245	210	225
Printing speed (mm/s)	20	35	30
Retraction (mm)	5	6	16

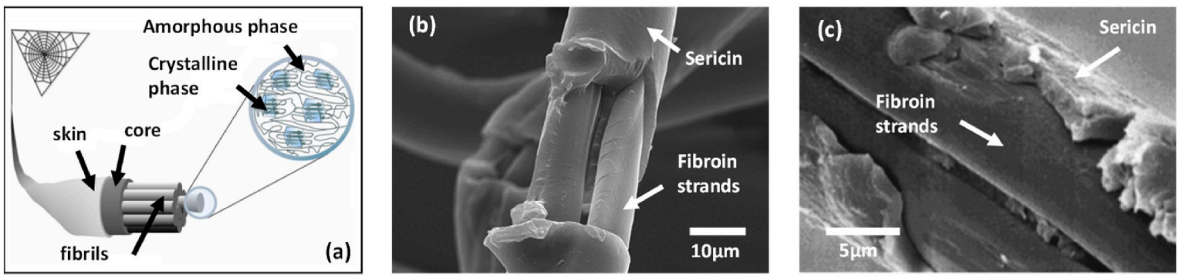

Fig. 1. (a) Schematic figure revealing the core-shell structure of spider silk fiber, adapted from Ref. [30]. (b–c) Longitudinal view captured through Scanning Electron Microscopy (SEM) unveils the intricate core-shell structure of cocoon silk fibers, adapted from Refs. [35,38].

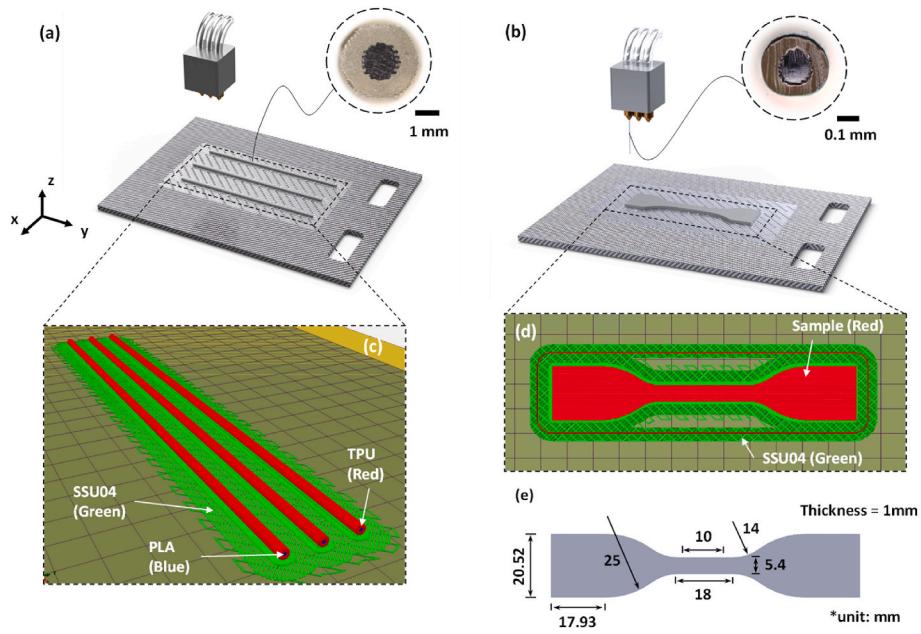

Fig. 2. (a) Fabrication of dual-phase CSAF by FDM printing. Optical microscopy image presents the internal structure and morphology of the core (black) - shell (transparent) filament. (b) Fabrication of samples using dual-phase CSAF. Optical microscopy image reveals a cross-sectional view of the bead purged from the nozzle. The volume fraction and geometric configuration of the core and shell materials within the filament and purged bead exhibit remarkable congruity. (c) Printing preface of dual-phase CSAFs in the slicing software, showing the arrangement of supporting material SSU04, soft shell material TPU, and stiff core material PLA. (d) Printing preface of dogbone sample in the slicing software, showing the printing path and raster orientation of the samples. (e) Dogbone sample size according to standard ASTM D638-14.

$$R = VD\rho/\mu \quad (1)$$

Where V is flow velocity, D is diameter, ρ is density and μ is viscosity. R is Reynolds number and it is a dimensionless value. The viscosity coefficients of PLA and TPU under the same printing temperature are on the same order of magnitude [50,51]. Despite the small difference of materials viscosity, upon substituting the value into equation (1), the flow type of the extruded bead can be characterized as laminar flow. Therefore, the architectural hierarchy of materials remains consistent after extrusion. Fig. 2 (b) presents the fabrication process of the samples, accompanied by optical microscopy image displaying the cross-section of the purged bead for CSAF-PLA34 %. The image clearly demonstrates the congruity between CASF and purged bead in the material and geometrical configuration.

To adhere to standard testing procedures and ensure comparability, the geometry and dimension of specimens followed ASTM D638-14 Standard Test Method for Tensile Properties of Plastics [52]. Sheet tension test specimens Type IV was employed to study mechanical behaviors, and the geometry and dimension of specimens are presented in Fig. 2 (e). In this study, the primary focus is on the synergistic effects arising from core-shell structure within the printed bead. The effect from other structural hierarchy, such as weaving effect caused by raster orientation, shall be excluded. Therefore, as shown in Fig. 2 (d), the raster orientation was consistently set to 0° to ensure a parallel alignment with the load direction. Table 2 presents associated printing parameters, which ensure the production of high-quality specimens with different volume fractions.

2.4. Uniaxial tensile test

The uniaxial tensile tests were conducted using an MTS-Electromechanical tensile test machine equipped with a 5 kN load cell (MTS Systems Corporation). To capture and analyze the strain behavior of the samples, VIC-2D Digital Image Correlation (DIC) was employed. This imaging technique allowed for the measurement of strain within the gauge length of the samples over time.

Table 2
The printing parameters for printing samples.

Materials	SSU04	Dual-phase CSAFs
Filament diameter (mm)	2.85	2.85
Nozzle diameter (mm)	0.4	0.3
Extrusion width (mm)	0.6	0.3
1st layer thickness (mm)	0.6	0.1
Layer thickness (mm)	0.15	0.1
Heat bed temperature (°C)	60	60
Chamber temperature (°C)	30	30
Nozzle temperature (°C)	245	225
Printing speed (mm/s)	20	30
Retraction (mm)	5	16

In accordance with the ASTM D638-14 standard, different testing speeds were applied based on the sample material. The PLA samples were tested at a strain rate of 0.1 min^{-1}, while the TPU samples and the CSAF printed samples were tested at a strain rate of 1.5 min^{-1}. These speeds were chosen to ensure consistent and reliable results during the tension testing process.

2.5. Characterization

The internal structure of 3D printed dual-phase CSAF, the core-section of printed bead extruded from dual-phase CSAF, the inner architecture and fracture behavior of samples printed by dual-phase CSAF were observed by a digital optical microscope Hirox RH-2000.

3. Results and discussion

3.1. Mechanical behavior of dual-phase CSAF printed specimens

The tensile stress-strain curves of specimens are shown in Fig. 3 (a). Table 3 presents the mechanical properties of base materials and dual-phase CSAF printed specimens as a function of different volume fraction of core. The cross-section view of a specimen, as shown in Fig. 3(b

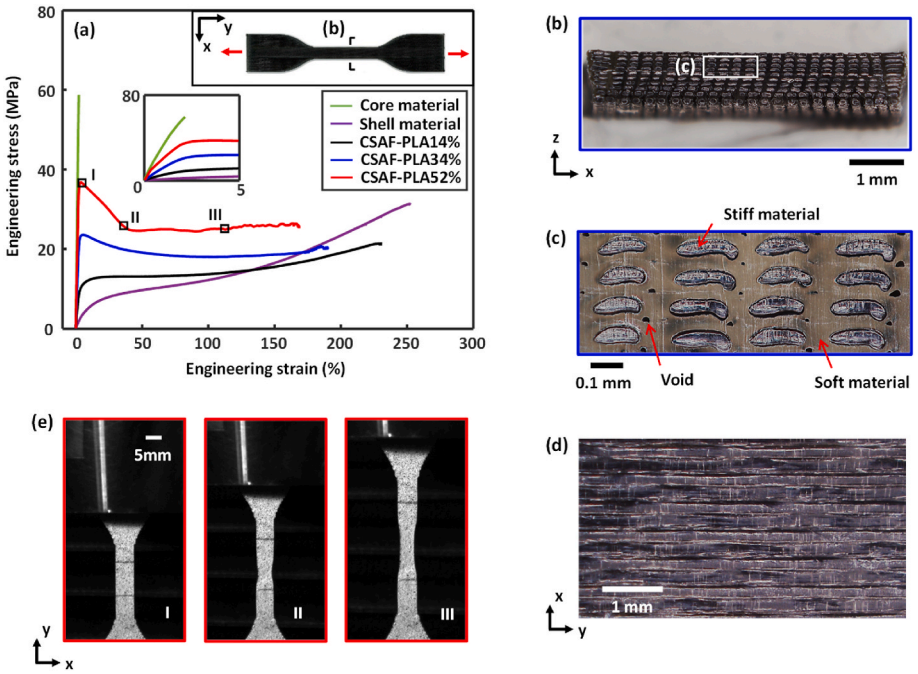

Fig. 3. (a) Stress-strain curves for the CSAF printed specimens with varying volume fractions and the single material filament printed samples of constituent materials (PLA and TPU). Cross-section view of the CSAF-PLA34 % printed sample before testing at (b) lower and (c) higher magnification. (d) Longitudinal view of the CSAF-PLA34 % printed sample after testing, showing the presence of uniformly distributed cracks. (e) Snapshots during testing, showing strain concentration and development within the gauge length.

Table 3
Mechanical properties of specimens under uniaxial tensile test.

Specimens (Volume fraction of Core)	Initial Young's modulus (MPa)	Yield strength (MPa)	Plateau stress (MPa)	Ultimate stress (MPa)	Ultimate strain (%)	Energy absorption capacity (MJ/m^3)
PLA	3307.2 ± 28.9	59.7 ± 3.0	–	59.7 ± 3.0	2.2 ± 0.1	0.7 ± 0.1
TPU	132.7 ± 7.2	7.8 ± 1.1	–	31.4 ± 1.8	253.3 ± 6.8	40.7 ± 3.7
CSAF-PLA14 %	510.4 ± 31.7	13.1 ± 1.2	13.1 ± 0.2	18.5 ± 2.5	232.6 ± 2.1	35.2 ± 0.5
CSAF-PLA34 %	1177.3 ± 49.0	23.6 ± 0.7	18.1 ± 0.1	20.4 ± 0.6	186.5 ± 5.5	36.7 ± 0.1
CSAF-PLA52 %	1991.4 ± 67.7	36.8 ± 1.5	24.9 ± 0.2	26.2 ± 0.5	164.6 ± 2.0	44.7 ± 0.2

and c), reveals that the mesostructure is well-fabricated and is consistent with the intended design. The core-shell structure is oriented parallel to the load direction by carefully controlling the printing path. Notably, there was minimal presence of deposition defects such as voids or misalignments in the specimen. It is important to acknowledge that these defects have the potential to decrease the mechanical performance of the printed specimens. To mitigate the influence of deposition defects on the mechanical performance, two strategies were employed—(i) increasing the overlap between adjacent printing paths; and (ii) reducing the gap between raft and the first layer. By implementing these strategies, the negative impact of deposition defects has been largely minimized.

The dual-phase CSAF printed specimens exhibit much higher ultimate strain and energy absorption—the area under stress-strain curve—than the core material. Specifically, the specimens printed from CSAF-PLA14 %, CSAF-PLA34 %, and CSAF-PLA52 % exhibit energy absorption capacities of 35.2 ± 0.5 MJ/m^3, 36.7 ± 0.1 MJ/m^3, and 44.7 ± 0.2 MJ/m^3, respectively, whereas the core material only achieves a capacity of 0.7 ± 0.1 MJ/m^3. Interestingly, the CSAF printed specimens also exhibit higher energy absorption capacity than the tough shell material of same volume. This phenomenon can be attributed to the occurrence of a large number of cracks within hard core material, bonding failure and slip between both materials. Moreover, the CSAF printed specimens display notable increases in the initial elastic modulus compared to the shell material. The shell material exhibits an initial elastic modulus of 132.7 ± 7.2 MPa, while the samples of CSAF-PLA14 %, CSAF-PLA34 %, and CSAF-PLA52 % demonstrate initial elastic modulus of 510.4 ± 31.7 MPa, 1177.31 ± 49.0 MPa, and 1991.4 ± 67.7 MPa, respectively. This significant improvement indicates the superior mechanical properties of the CSAF printed specimens in initial elastic modulus compared to the shell material and in energy absorption capacity compared to the core material.

A typical stress-strain curve of a CSAF printed specimen, printed from CSAF-PLA34 %, exhibits four distinct stages: (I) initial linear-elastic stage, (II) stress-softening process, (III) stress plateau, and (IV) stress hardening stage prior to rupture. In the case of a high core material volume fraction (CSAF-PLA 52 %), the stress hardening stage (IV) is difficult to be observed. This could be attributed to the fact that the plateau stress is in close proximity to the rupture stress. The proximity of these two stress levels limits the observable duration of the stress hardening stage.

A series of Digital Image Correlation (DIC) images captured during the testing of the CSAF-PLA52 % printed specimen offers valuable insights into the progressive damage mechanism inherent in the core-shell structure, as illustrated in Fig. 4 I to VI. Initially, as deformation commences, the specimen enters a linear-elastic stage (I), depicted in Fig. 4 I and II. Upon surpassing the failure strain of the core (Fig. 4 II), the necking phenomenon ensues, correlating with the stress-softening stage (II) observed in the stress-strain curve. Throughout this phase, partial damage initiates within the core and propagates laterally across the

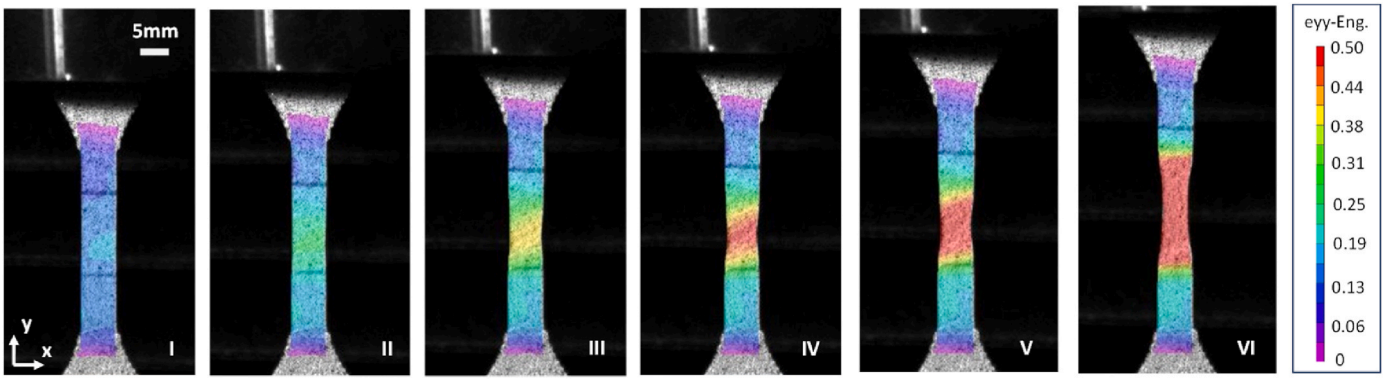

Fig. 4. DIC results of snapshot I to VI during testing, revealing the concentration and development of strain within the gauge length. Images I and II represent the linear-elastic stage; Images II to IV depict the stress-softening stage; Images IV to VI illustrate the stress plateau stage.

cross-section, as evidenced by images II to IV in Fig. 4. Concurrently, the soft shell undergoes stretching within the partially damaged zones. As the undamaged area of the core diminishes within the critical cross-section, the stress exhibits a decreasing trend. Following lateral propagation, partial damage progresses longitudinally along the load direction, marking the onset of the stress plateau stage. During this stage, the damage zone expands into the undamaged zone along the load direction as the critical cross-section traverses the entire gauge length, as depicted by DIC images IV to VI in Fig. 4. The global stress profile is influenced by the progressive cracking of the core on the critical cross-section as it advances longitudinally along the load direction. The growth of local strain is primarily driven by the stretch of shell in the damage zone. At the end of stress pleatue stage (III), the damage zone covers the entire gauge length. In stress hardening stage (IV), the overall strain is contributed by the stretching of the undamaged shell within the entire gauge length. When the local material of shell reaches its ultimate strain, overall rupture happens. Fig. 3 (d) presents the longitudinal view of a CSAF printed specimen after uniaxial test. Numerous uniformly distributed sub-cracks are observed. Unlike brittle failure which usually involves the formation of a primary crack through the entire cross-section leading to the failure, this damage mode makes full use of the effectiveness in stress resistance of all the materials involved.

It is important to note that materials tend to exhibit more brittle behavior and higher strength at higher strain rates, attributed to limited time for dislocation motion and deformation mechanisms. Conversely, lower strain rates may lead to increased creep deformation and reduced strength, particularly in materials susceptible to time-dependent processes like creep and stress relaxation. For CSAF printed specimens, high strain rates may lead to brittle failure due to limited time for continuous damage mechanisms to occur. Failure of the soft shell may coincide with the breakage of the stiff core, as the former experiences higher stretch and stress without sufficient time for shear-lag effect to transmit load to the undamaged core. Understanding these strain rate effects is crucial for optimizing the performance of bi-material filaments in various applications.

3.2. Damage mechanism

A theoretical model is proposed to understand the mechanical behavior of the core-shell structure under uniaxial tensile loading. The nature of stiff core and tough shell impart high stiffness and toughness to the core-shell structure. Taking a unit cell out from CSAF printed specimens, and for simplicity, a cylindrical core-shell model is considered, as shown in Fig. 5 (b). During the process of tension, stiff core takes the main load while soft shell takes the main stretch. Shear stress between the core and the shell transfers axial load. The loading history of the core-shell structure can be divided into three stages: (I) elastic deformation stage. (II) core-dominated continuous damage stage (III) shell-dominated stretching stage before collapse, as sketched in Fig. 5 (a).

At the initial tensile loading, both core and shell of CASF printed specimens experience elastic deformation stage. The elastic modulus of both materials is assumed to be constant within this stage. The initial effective stiffness of core-shell structure can be formulated by rule of mixture, as described by equation (2).

$$E_o = (1 - \varphi_c)E_s + \varphi_c E_c \tag{2}$$

where E_o is the effective stiffness of core-shell structure, E_s and E_c are initial elastic modulus of shell material and core material, respectively. φ_c is volume fraction of core material.

$$f_1 = E_o \varepsilon_o \tag{3}$$

where f_1 is the first peak strength as shown in Fig. 5 (a); ε_o is failure strain of core material.

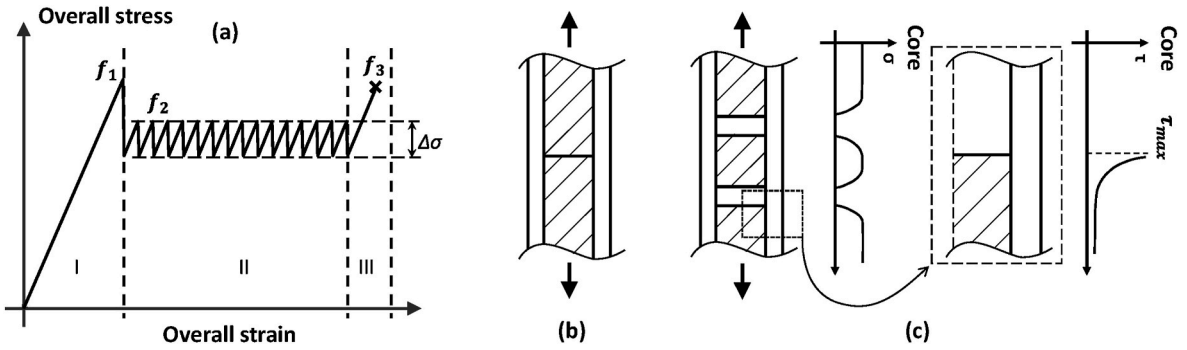

Fig. 5. (a) Sketch of stress-strain curve of core-shell structure, divided into three stages. (b) The sketch model of initial crack mechanism that occurs at the end of stage I (c) The sketch model of continuous cracks mechanism that occurs in stage II.

By equation (2), it is obvious to found that the effective stiffness of core-shell structure is determined by two nondimensional parameters—(i) the Young's modulus ratio between shell material and core material and (2) the volume fraction of core material. Within a fixed ratio, the effective stiffness of core-shell structure has a linear relationship with the volume fraction of core material.

After core material reaches fracture strain, crack occurs in core material while high ultimate strength of shell material prevents the core-shell structure from catastrophe failure. During this stage, the stiff core undergoes locally continuous damage in the tensile direction, while the shell in core damage zone is heavily stretched and undamaged as it has not reached its failure strength. After the stiff core breaks locally, the soft-shell surrounding holds the stretch, thereby giving rise to a stress realization. As the soft shell at the damage zone continues to elongate, the stress in the undamaged core material near the crack also increases. When it reaches the failure criteria, a new crack initiates. This phenomenon is manifested as a serrated plateau region in stress-strain curve, as shown in Fig. 5 (a) stage II.

When the initial crack has formed, the subsequent damage mechanism differs with the initial crack. The initial crack occurs under a uniform tensile stress condition, while the subsequent cracks occur in core material due to the tensile stress transferred from stretched shell and shear stress between both materials, as shown in Fig. 5 (b) and (c). To demonstrate its mechanism, shear-lag model is exploited in this study. During the process of continuous damage, tensile loading is transferred from the shell to the core through shear stress between the shell and the core [53]. Fig. 5 (c) shows the sketched distribution of shear stress. Significant stress peak occurs at the ends of the joint of materials. The maximum shear stress can be estimated by equation (4). It approximates to a constant value with long joints. The derivation is proved in supplementary information S1.

$$\tau_{max} = \frac{P}{S}\lambda = k_1\sigma_o \tag{4}$$

where τ_{max} is the maximum shear stress between the joint of both materials. P is the axial force acting on the entire core-shell structure. S is the contact perimeter of both materials. σ_o is the engineering axial stress of the entire core-shell structure, $\sigma_o = P/A_o$ A_o is the cross-section area of the entire structure. k_1 is a factor used to measure the relationship between the axial stress of entire core-shell structure and the maximum shear stress between both materials. $k_1 = \mathrm{r_c}\lambda/2\varphi_c$. $\mathrm{r_c}$ is the radius of core material. φ_c is the volume fraction of core material. λ^{-1} is the characteristic length for the necessary distance to transfer the load. It can be calculated by equation (5).

$$\lambda = \sqrt{\frac{G_s}{h}\frac{\mathrm{E_c r_c}}{\mathrm{E_s t_s}}\left(\frac{1}{\mathrm{E_s t_s} + \mathrm{E_c r_c}}\right)} \tag{5}$$

where G_s is the shear modulus of shell material. $\mathrm{t_s}$ is the thickness of shell material for tension deformation. h is the thickness of shell material for shear deformation. The irregular distribution of shear stress poses a challenge in characterizing the shear deformation of the soft shell material. To address this issue, a parameter α is introduced to define the thickness of an effective layer of the soft shell subjected to uniform shear stress at the material interface. The parameter α ranges from 0 to 1, and it's crucial to note that its value may change during the stretching process. Consequently, the thickness of the shell material undergoing shear deformation is expressed as $h = \alpha(\mathrm{r} - \mathrm{r_c})$. The remaining portion of the shell material is presumed to undergo tensile deformation, denoted as $\mathrm{t_s} = (1-\alpha)(\mathrm{r} - \mathrm{r_c})$.

Considering the brittleness of core material, once one of the tension stress and shear stress in core material reaches the resistance of material nature, damage is assumed to occur in core material. The damage initiation criterion can be written as equation (6).

$$\max\left\{\frac{\tau_{max}}{\tau_1}, \frac{\sigma_c}{\sigma_1}\right\} = 1 \tag{6}$$

where τ_1 and σ_1 are the shear strength and tensile strength of core material. The maximum stress failure criterion is applied for core material due to its brittleness. The relationship between the tensile strength σ_1 and the shear strength τ_1 of core material can be denoted as $\sigma_1 = \frac{1}{n}\tau_1 = f_c$, where n is the ratio of shear strength to tensile strength, and f_c presents the maximum strength of core material. Experimental studies have indicated that the shear strength of PLA is approximately 0.8–0.9 times the tensile strength [61–63].

To avoid catastrophic failure occurring in stage II, the stress resistance of shell material should meet following requirement.

$$\frac{f_s}{f_c} \geq \min\left\{\frac{1}{\mathrm{k_3}}, \frac{n}{\mathrm{k_1 k_2 k_3}}\right\} \tag{7}$$

where f_s is the ultimate strength of shell material. $\mathrm{k_2}$ is a factor used to measure the relationship between the axial stress of entire structure and the axial stress in core material at the undamaged zone, $\sigma_o = \mathrm{k_2}\sigma_c$. $\mathrm{k_2} = \varphi_c + \frac{\mathrm{E_s}}{\mathrm{E_c}}(1-\varphi_c)$. $\mathrm{k_3}$ is a factor used to measure the relationship between the axial stress in shell material at damage zone and axial stress in core material at the undamaged zone, $\sigma_c = \mathrm{k_3}\sigma_s$. $\mathrm{k_3} = (1-\varphi_c)/\varphi_c$. The plateau stress f_2 non-dimensionalized by first peak stress is expressed as followed.

$$\frac{f_2}{f_1} \leq \min\left\{1, \frac{n}{\mathrm{k_1 k_2}}\right\} \tag{8}$$

When the core material ruptures, the stress previously borne by the undamaged core is suddenly released, leading to a relaxation of deformation within the material. This results in an overall decrease in stress within the structure, as shown in Fig. 5 (a). As the stress is released from the core material, the shell material at the rupture area undergoes immediate stretching. Through the shear-lag effect, the axial stress experienced by the shell material is transmitted to the undamaged core material, leading to continuous damage propagation. This dynamic interplay between the core and shell materials highlights the significance of stress redistribution and relaxation mechanisms in influencing the overall mechanical response. It's worth noting that the overall stress drop during this process is influenced by several factors, as elaborated below.

$$\Delta\sigma \propto \frac{\mathrm{E_c}}{\mathrm{E_s}}, \frac{1}{\varphi_s}, \frac{\mathrm{A_c}}{S}, \frac{t}{L}, h\omega' \tag{9}$$

where $\varphi_s = 1 - \varphi_c$ is the volume fraction of shell material. A_c is the cross-section area of core. L is the overall length of structure. t is the length of shell material in damage zone.

It can be observed that the plateau stress in stage II, as well as stress drop, is influenced by mechanical properties of materials, material proportion, structure geometry and size, etc. Due to the significant shear stress present in critical stress state of stage II, the plateau stress f_2 can only be less than or equal to the first break stress f_1. Increasing the ratio of contact area to the cross-section area of core is a strategy to enhance the plateau stress and reduce stress drop.

When the entire core is fractured into numerous smallest segments, it becomes difficult for the stress in the core to reach the failure criterion. Therefore, no crack will happen, and the deformation goes into stage III. The elongation is taken by the shell until it fails. When the shell reaches its ultimate strength, this structure undergoes overall failure.

$$f_3 = (1-\varphi_c)f_s \tag{10}$$

The ultimate strength of this strength is estimated as equation (10).

It is important to note that this deduction is based on the simplification that only uniaxial stresses and shear stress in the longitudinal direction are considered, while the radial stress in the transverse

direction is neglected. In the damaged segment, the high tensile stress present in the shell material and the low tensile stress in the core material cause the shell material to contract radially, resulting in high radial tensile stress in the core material around the interface. In the undamaged segment, the core material bears longitudinal tensile stress while the shell material experiences low longitudinal tensile stress. This leads to radial contraction in the core material and high compressive stress in the core material. These high radial tensile and compressive stresses may induce failure in the core material or compromise the bonding at the interface. Due to the complex stress distribution, deducing an exact failure criterion poses a challenge. In this study, we make the assumption that materials fail under uniaxial stresses, and the adhesion remains undamaged.

3.3. Numerical analysis

The material properties obtained from experiments were utilized to perform numerical simulations using commercial software Abaqus 2019. Three simplified Representative Volume Elements (RVEs) representing core-shell fiber with a 0.3 mm diameter were constructed, using 2D axisymmetric modeling to homogenize the properties of CSAF printed samples with varying volume fractions. The elastic material model was employed for core material, while for the shell material, a hyperelastic Ogden model was employed, fitted with TPU tested in experiment (the purple curve in Fig. 6 (a)). Continuous damage mechanisms were integrated using cohesive elements to simulate crack initiation and propagation. The failure of cohesive element is fitted with PLA tested in experiment (the green curve in Fig. 6 (a)). The crack gap was established as the critical length λ^{-1} corresponding to each specific case. The overall length of the RVE model is sufficient to accommodate more than ten cracks. The core material was modeled with 4-node axisymmetric quadrilateral elements (CAX4), while the shell material utilized 4-node axisymmetric quadrilateral elements with a hybrid formulation (CAX4H). The cracks were pre-set at where the damage is expected to occur by 4-node axisymmetric cohesive element (COHAX4). The models were analyzed through static general implicit analysis with nonlinear geometry activated.

The simulation results of the RVE models are depicted in Fig. 6 (a) and (b). In Fig. 6 (a), a similar trend to the experimental results is observed. The stress-strain curve of the RVE model with low PLA volume fraction (CSAF-PLA14 %) exhibits a linear stage followed by a stress plateau stage. Conversely, in the case of high PLA volume fraction RVE models (CSAF-PLA34 % and CSAF-PLA52 %), there is no stress-softening stage (II); instead, the stress drops dramatically to the platform stage after the linear stage. As the RVE model simulates only one line of core-shell fiber and experiences solely longitudinal damage propagation, only the stress plateau stage (III) is observed. This verifies that lateral damage propagation within the specimen causes the stress-softening stage (II), while longitudinal damage propagation leads to the stress plateau stage (III). Fig. 6b presents the RVE models with high (CSAF-PLA52 %) and low (CASF-PLA14 %) PLA volume fractions. Two types of damage, fracture mode II (sliding mode) and fracture mode I (opening mode), are observed in cases of high and low PLA volume fractions. In the CSAF-PLA52 % RVE model, crack initiation consistently occurs in proximity to pre-existing cracks, as the material failure mechanism is governed by shear stress, with the highest shear stress concentration located around these existing cracks. Conversely, in the CSAF-PLA14 % RVE model, cracks initiate due to tensile stress, resulting in a random distribution of crack positions far from existing cracks.

By incorporating the material properties obtained from experiments into the theoretical analysis, comparisons are made among the results of the theoretical model, numerical model, and experiments. The results of analytical model, numerical models, and experiment have good agreement, as showed in Fig. 7 (a) and (b). As the results indicate, the initial effective stiffness E_o and first peak stress f_1 of dual-phase CSAF printed specimens show a proportional relationship with the core material volume fraction φ_c. The relationship of f_2/f_1 and f_s/f_c with φ_c vary depending on the values of α. Fig. 7 (c) displays two curves corresponding to α values of 0.1 and 0.5. These curves represent envelope curves for different α values. The curve of f_2/f_1 as a function of φ_c shifts to the right as α value increases. It reaches its rightmost position when $\alpha = 0.5$. Interestingly, when α exceeds 0.5, the curve shifts back to the left with further increases in α. In cases with low core material volume fractions, the plateau stress equals the first peak stress due to continuous breakage in stage II, resulting from axial tensile failure in the core material. However, for cases with high volume fractions of core, the plateau stress is smaller than the first peak stress, attributed to the shear failure in the core. This difference is a consequence of the continuous increase in the ratio of the maximum shear stress to the axial stress as the volume fraction of core rises. This trend is consistent with experimental and numerical results. Fig. 7 (d) illustrates the selection of the engineering ultimate tensile strength of the shell material based on the strength of the core material. The upper bound corresponds to the curve when α equals 0.5. It is evident that the required engineering ultimate strength of the shell material increases with an increase in the volume fraction of core.

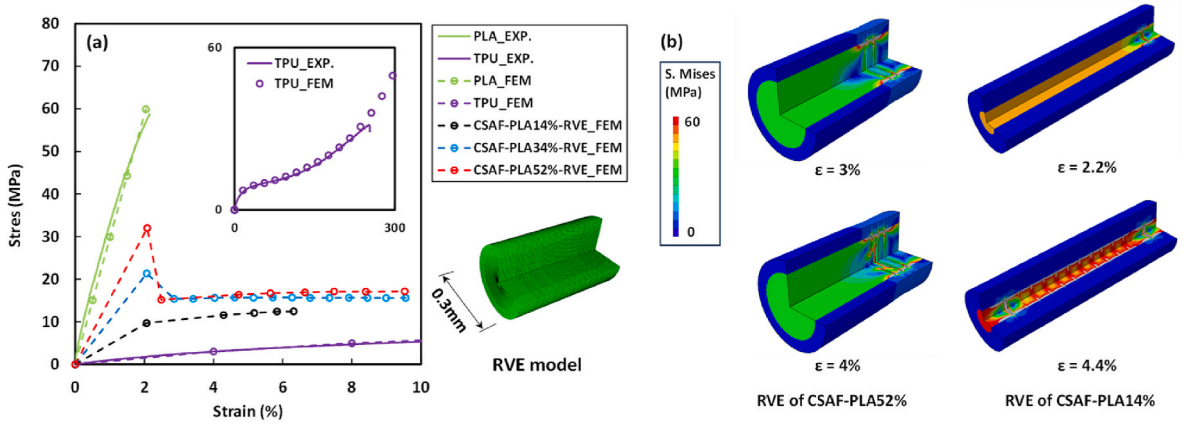

Fig. 6. (a) Material property curves for PLA (green) and TPU (purple) fitted with experimental results, along with simulation results from the RVE model for different PLA volume fractions: 14 % (black), 34 % (blue), and 52 % (red). (b) Two RVE models depicting high and low PLA volume fractions, illustrating two distinct types of damage: continuous cracks due to shear failure in core material at high PLA volume fractions (CSAF-PLA52 %), and discrete cracks due to tensile failure in core material at low PLA volume fractions (CSAF-PLA14 %). (For interpretation of the references to colour in this figure legend, the reader is referred to the Web version of this article.)

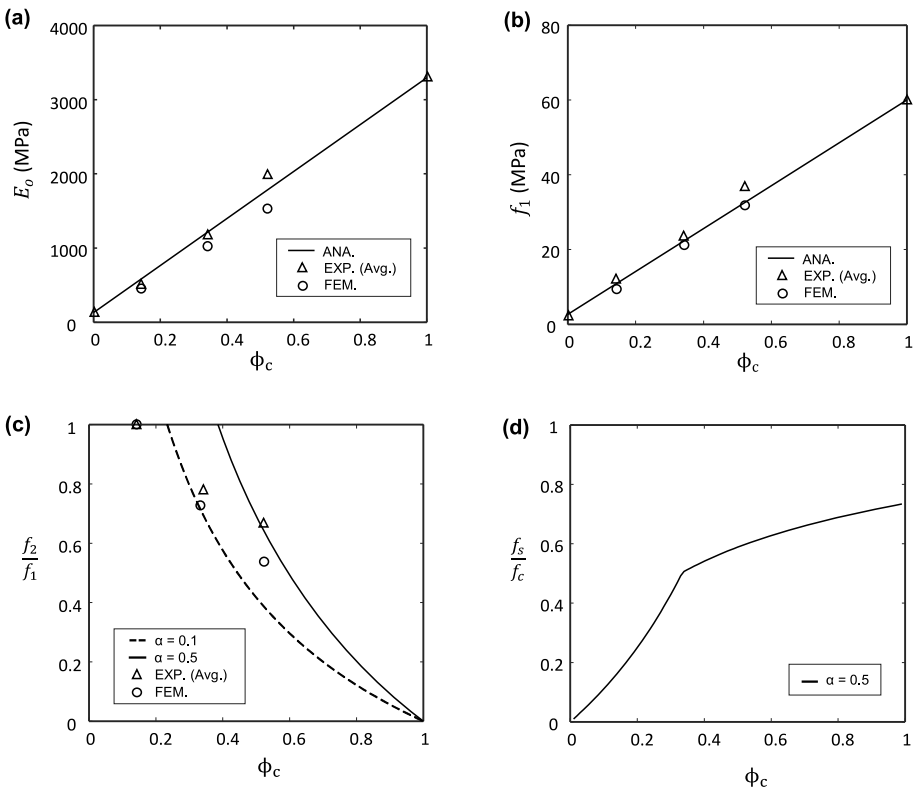

Fig. 7. The plot of the (a) initial effective stiffness and (b) first peak stress of samples with respect to core material volume fraction based on analysis and experimental results. (c) The curves of the ratio of the plateau stress f_2 and first peak stress f_1 with respect to core material volume fraction under different α values. (d) The curves of the ratio of the shell material ultimate tensile strength f_s and the core material ultimate tensile strength f_c with respect to core material volume fraction. The selection of shell material ultimate tensile strength shall be above the curve.

4. Conclusions

In summary, this work proposes a bio-inspired multimaterial core-shell architectured design for FDM filament. The printed specimens using dual-phase CSAFs exhibit enhanced mechanical properties—higher stiffness, and toughness—compared to their constituent materials. For instance, compared with core material, the CSAF printed specimens increase up to ~61 folds in toughness (from 0.7 ± 0.1 MJ/m^3 to 44.7 ± 0.2 MJ/m^3). When compared with shell material, the CSAF printed specimens show slight increase of ~9 % in toughness (44.7 ± 0.2 MJ/m^3 and 40.7 ± 3.7 MJ/m^3), and significant increase up to ~14 folds in initial elastic modulus (1991.4 ± 67.7 MPa and 132.7 ± 7.2 MPa). The loading history of the CSAF printed sample presents the typical four stages: (I) the initial linear-elastic stage before damage occurs, (II) the softening process while damage in core material laterally progress in the direction perpendicular to the loading direction, (III) the stress plateau while damage longitudinally progress in the direction parallel with the loading direction, and (IV) the stress hardening stage contributed to the stretch of undamaged shell material. A theoretical model based on a simplified cylindrical core-shell unit cell is introduced to elucidate the characteristic values of the loading history. FE models are built based on the theoretical model, and the FE results show good agreement with the experiment results. The theoretical model also provides the selection of materials according to its ultimate strength.

The findings of this work enlighten an idea of method to contribute to an enhancement in toughness for materials characterized by high stiffness and strength but prone to brittleness, and on the other hand, lead to an increase in initial stiffness for materials displaying high toughness but possessing low initial stiffness and demonstrating flexibility. Table 4 presents the tensile mechanical properties obtained in this

Table 4
Approximate tensile mechanical properties for monolithic, composite materials and inner designed architecture used in FDM.

Structure	Materials	Tensile modulus (MPa)	Tensile strength at yield (MPa)	Tensile elongation at break (%)	Energy absorption capacity (MJ/m^3)	Reference
Monolithic materials	PEEK	3120	85	26	1.5	[54]
	ABS	1940	49.7	7.5	0.9	[55]
	Nylon	1000	37	243	72	[56]
	PLA	3307	59.7	2	0.7	
	PLA	3139	50.9	–	–	[59,60]
	TPU	133	1.8	253.3	40.7	
Silk inspired Core-Shell	**PLA52%-TPU**	**1991**	**36.8**	**164.6**	**45**	
Compounding	PLA50%-TPU	1000	27.3	27	5.6	[57]
Plywood	PLA	3285	55	3.1	1.3	[18]
Sandwich	PLA-ABS-PLA	1600	43	5.3	1.4	[58]

study and in previous research on monolithic materials [54–56], composite materials used for FDM [57] and materials with inner designed architecture printed by FDM [18,58]. Commonly, monolithic materials possess either high stiffness or high energy absorption capacity. While material modification, inner structure design, and other hybrid methods are proposed for enhancing stiffness and ductility. The result of this work demonstrates the superiority of inner architecture in enhancing the mechanical properties of multi-material composite, compared to material compounding. And compared to other inner structure design, the bio-inspired core-shell design presents superior improvement in elongation and energy absorption capacity. Moreover, this bioinspired core-shell design has potential to be applied to other high-performance and functional materials.

CRediT authorship contribution statement

Li Liang: Formal analysis, Investigation, Methodology, Validation, Writing – original draft, Writing – review & editing. **Filippo Berto:** Resources, Writing – review & editing. **Chao Gao:** Conceptualization, Formal analysis, Funding acquisition, Investigation, Methodology, Supervision, Validation, Writing – review & editing.

Declaration of competing interest

The authors declare that they have no known competing financial interests or personal relationships that could have appeared to influence the work reported in this paper.

Data availability

Data will be made available on request.

Acknowledgements

This work was partially supported by NTNU Discovery (Grant No. 90427500).

Appendix A. Supplementary data

Supplementary data to this article can be found online at https://doi.org/10.1016/j.compositesb.2024.111474.

References

[1] Barthelat F. Architectured materials in engineering and biology: fabrication, structure, mechanics and performance. Int Mater Rev 2015;60(8):413–30. https://doi.org/10.1179/1743280415Y.0000000008.
[2] Abu Samk K, Hibbard GD. Microtruss composites. In: Estrin Y, Bréchet Y, Dunlop J, Fratzl P, editors. Architectured materials in nature and engineering: archimats. Cham: Springer International Publishing; 2019. p. 1–21. https://doi.org/10.1007/978-3-030-11942-3_1.
[3] Ashby M. Designing architectured materials. Scripta Mater 2013;68(1):4–7. https://doi.org/10.1016/j.scriptamat.2012.04.033.
[4] Ashby MF, Bréchet YJM. Designing hybrid materials. Acta Mater 2003;51(19):5801–21. https://doi.org/10.1016/S1359-6454(03)00441-5.
[5] Xia Z. Biomimetic principles and design of advanced engineering materials. John Wiley & Sons; 2016.
[6] Lin AY-M, Meyers MA. Interfacial shear strength in abalone nacre. J Mech Behav Biomed Mater 2009;2(6):607–12. https://doi.org/10.1016/j.jmbbm.2009.04.003.
[7] Barthelat F, Tang H, Zavattieri PD, Li CM, Espinosa HD. On the mechanics of mother-of-pearl: a key feature in the material hierarchical structure. J Mech Phys Solid 2007;55(2):306–37. https://doi.org/10.1016/j.jmps.2006.07.007.
[8] Chen J, Zu Q, Wu G, Xie J, Tuo W. Review of beetle forewing structures and their biomimetic applications in China: (II) on the three-dimensional structure, modeling and imitation. Mater Sci Eng C 2015;55:620–33. https://doi.org/10.1016/j.msec.2015.04.045.
[9] Lomakin J, Huber PA, Eichler C, Arakane Y, Kramer KJ, Beeman RW, et al. Mechanical properties of the beetle elytron, a biological composite material. Biomacromolecules 2011;12(2):321–35. https://doi.org/10.1021/bm1009156.
[10] Lomakin J, Arakane Y, Kramer KJ, Beeman RW, Kanost MR, Gehrke SH. Mechanical properties of elytra from Tribolium castaneum wild-type and body color mutant strains. J Insect Physiol 2010;56(12):1901–6. https://doi.org/10.1016/j.jinsphys.2010.08.012.
[11] Allahyari P, Silani M, Yaghoubi V, Milovanovic P, Schmidt FN, Busse B, et al. On the fracture behavior of cortical bone microstructure: the effects of morphology and material characteristics of bone structural components. J Mech Behav Biomed Mater 2023;137:105530. https://doi.org/10.1016/j.jmbbm.2022.105530.
[12] Zimmermann EA, Ritchie RO. Bone as a structural material. Adv Healthcare Mater 2015;4(9):1287–304. https://doi.org/10.1002/adhm.201500070.
[13] Wegst UGK, Bai H, Saiz E, Tomsia AP, Ritchie RO. Bioinspired structural materials. Nat Mater 2015;14(1):23–36. https://doi.org/10.1038/nmat4089.
[14] Ortiz C, Boyce MC. Bioinspired structural materials. Science 2008;319(5866):1053–4. https://doi.org/10.1126/science.1154295.
[15] Naleway SE, Porter MM, McKittrick J, Meyers MA. Structural design elements in biological materials: application to bioinspiration. Adv Mater 2015;27(37):5455–76. https://doi.org/10.1002/adma.201502403.
[16] Guo C, Song W, Dai Z. Structural design inspired by beetle elytra and its mechanical properties. Chin Sci Bull 2012;57(8):941–7. https://doi.org/10.1007/s11434-011-4956-3.
[17] Zhang Y, Zhang F, Yan Z, Ma Q, Li X, Huang Y, et al. Printing, folding and assembly methods for forming 3D mesostructures in advanced materials. Nat Rev Mater 2017;2(4):17019. https://doi.org/10.1038/natrevmats.2017.19.
[18] Sun Y, Tian W, Zhang T, Chen P, Li M. Strength and toughness enhancement in 3d printing via bioinspired tool path. Mater Des 2020;185:108239. https://doi.org/10.1016/j.matdes.2019.108239.
[19] Liu Q, Hong L, Dong X, Zhai W. 3D printed hierarchical interpenetrating phase composites with multi-scale mechanical energy absorption mechanisms. Compos B Eng 2023;264:110911. https://doi.org/10.1016/j.compositesb.2023.110911.
[20] Yaraghi NA, Guarín-Zapata N, Grunenfelder LK, Hintsala E, Bhowmick S, Hiller JM, et al. A sinusoidally architected helicoidal biocomposite. Adv Mater 2016;28(32):6835–44. https://doi.org/10.1002/adma.201600786.
[21] Nazir A, Gokcekaya O, Md Masum Billah K, Ertugrul O, Jiang J, Sun J, et al. Multi-material additive manufacturing: a systematic review of design, properties, applications, challenges, and 3D printing of materials and cellular metamaterials. Mater Des 2023;226:111661. https://doi.org/10.1016/j.matdes.2023.111661.
[22] Wang Y, Li X. 4D-printed bi-material composite laminate for manufacturing reversible shape-change structures. Compos B Eng 2021;219:108918. https://doi.org/10.1016/j.compositesb.2021.108918.
[23] Tran P, Ngo TD, Ghazlan A, Hui D. Bimaterial 3D printing and numerical analysis of bio-inspired composite structures under in-plane and transverse loadings. Compos B Eng 2017;108:210–23. https://doi.org/10.1016/j.compositesb.2016.09.083.
[24] Ko K, Jin S, Lee SE, Lee I, Hong J-W. Bio-inspired bimaterial composites patterned using three-dimensional printing. Compos B Eng 2019;165:594–603. https://doi.org/10.1016/j.compositesb.2019.02.008.
[25] Yavas D, Liu Q, Zhang Z, Wu D. Design and fabrication of architected multi-material lattices with tunable stiffness, strength, and energy absorption. Mater Des 2022;217:110613. https://doi.org/10.1016/j.matdes.2022.110613.
[26] Jiang H, Le Barbenchon L, Bednarcyk BA, Scarpa F, Chen Y. Bioinspired multilayered cellular composites with enhanced energy absorption and shape recovery. Addit Manuf 2020;36:101430. https://doi.org/10.1016/j.addma.2020.101430.
[27] Compton BG, Lewis JA. 3D-Printing of lightweight cellular composites. Adv Mater 2014;26(34):5930–5. https://doi.org/10.1002/adma.201401804.
[28] Dimas LS, Bratzel GH, Eylon I, Buehler MJ. Tough composites inspired by mineralized natural materials: computation, 3D printing, and testing. Adv Funct Mater 2013;23(36):4629–38. https://doi.org/10.1002/adfm.201300215.
[29] Blackledge TA, Hayashi CY. Unraveling the mechanical properties of composite silk threads spun by cribellate orb-weaving spiders. J Exp Biol 2006;209(16):3131–40. https://doi.org/10.1242/jeb.02327.
[30] Blackledge TA. Spider silk: molecular structure and function in webs. In: Nentwig W, editor. Spider ecophysiology. Berlin, Heidelberg: Springer Berlin Heidelberg; 2013. p. 267–81. https://doi.org/10.1007/978-3-642-33989-9_20.
[31] Kluge JA, Rabotyagova O, Leisk GG, Kaplan DL. Spider silks and their applications. Trends Biotechnol 2008;26(5):244–51. https://doi.org/10.1016/j.tibtech.2008.02.006.
[32] Humenik M, Smith AM, Scheibel T. Recombinant spider silks—biopolymers with potential for future applications. Polymers 2011;3(1):640–61. https://www.mdpi.com/2073-4360/3/1/640.
[33] Papadopoulos P, Sölter J, Kremer F. Hierarchies in the structural organization of spider silk—a quantitative model. Colloid Polym Sci 2009;287(2):231–6. https://doi.org/10.1007/s00396-008-1968-x.
[34] Meyers MA, Chen P-Y, Lin AY-M, Seki Y. Biological materials: structure and mechanical properties. Prog Mater Sci 2008;53(1):1–206. https://doi.org/10.1016/j.pmatsci.2007.05.002.
[35] Murugesh Babu K. 13 - silk from silkworms and spiders as high-performance fibers. In: Bhat G, editor. Structure and properties of high-performance fibers. Oxford: Woodhead Publishing; 2017. p. 327–66. https://doi.org/10.1016/B978-0-08-100550-7.00013-9.
[36] Hardy JG, Römer LM, Scheibel TR. Polymeric materials based on silk proteins. Polymer 2008;49(20):4309–27. https://doi.org/10.1016/j.polymer.2008.08.006.
[37] Zhao H-P, Feng X-Q, Yu S-W, Cui W-Z, Zou F-Z. Mechanical properties of silkworm cocoons. Polymer 2005;46(21):9192–201. https://doi.org/10.1016/j.polymer.2005.07.004.
[38] Crivelli B, Perteghella S, Bari E, Sorrenti M, Tripodo G, Chlapanidas T, et al. Silk nanoparticles: from inert supports to bioactive natural carriers for drug delivery. Soft Matter 2018;14(4):546–57. https://doi.org/10.1039/C7SM01631J.

[39] Cheng P, Peng Y, Li S, Rao Y, Le Duigou A, Wang K, et al. 3D printed continuous fiber reinforced composite lightweight structures: a review and outlook. Compos B Eng 2023;250:110450. https://doi.org/10.1016/j.compositesb.2022.110450.
[40] Zhang Y, Qiao J, Zhang G, Li Y, Li L. Prediction of deformation and failure behavior of continuous fiber reinforced composite fabricated by additive manufacturing. Compos Struct 2021;265:113738. https://doi.org/10.1016/j.compstruct.2021.113738.
[41] Wang B, Ming Y, Zhou J, Xiao H, Wang F, Duan Y, et al. Fabrication of triangular corrugated structure using 3D printed continuous carbon fiber-reinforced thermosetting epoxy composites. Polym Test 2022;106:107469. https://doi.org/10.1016/j.polymertesting.2021.107469.
[42] Matsuzaki R, Ueda M, Namiki M, Jeong T-K, Asahara H, Horiguchi K, et al. Three-dimensional printing of continuous-fiber composites by in-nozzle impregnation. Sci Rep 2016;6(1):23058. https://doi.org/10.1038/srep23058.
[43] Tian X, Liu T, Yang C, Wang Q, Li D. Interface and performance of 3D printed continuous carbon fiber reinforced PLA composites. Compos Appl Sci Manuf 2016;88:198–205. https://doi.org/10.1016/j.compositesa.2016.05.032.
[44] Bodros E, Pillin I, Montrelay N, Baley C. Could b iopolymers reinforced by randomly scattered flax fibre be used in structural applications? Compos Sci Technol 2007;67(3):462–70. https://doi.org/10.1016/j.compscitech.2006.08.024.
[45] Shah DU. Developing plant fibre composites for structural applications by optimising composite parameters: a critical review. J Mater Sci 2013;48(18):6083–107. https://doi.org/10.1007/s10853-013-7458-7.
[46] Ho M-p, Wang H, Lee J-H, Ho C-k, Lau K-t, Leng J, et al. Critical factors on manufacturing processes of natural fibre composites. Compos B Eng 2012;43(8):3549–62. https://doi.org/10.1016/j.compositesb.2011.10.001.
[47] Darnal A, Shahid Z, Deshpande H, Kim J, Muliana A. Tuning mechanical properties of 3D printed composites with PLA:TPU programmable filaments. Compos Struct 2023;318:117075. https://doi.org/10.1016/j.compstruct.2023.117075.
[48] Balla VK, Kate KH, Satyavolu J, Singh P, Tadimeti JGD. Additive manufacturing of natural fiber reinforced polymer composites: processing and prospects. Compos B Eng 2019;174:106956. https://doi.org/10.1016/j.compositesb.2019.106956.
[49] Shashi Menon E. Chapter five - fluid flow in pipes. In: Shashi Menon E, editor. Transmission pipeline calculations and simulations manual. Boston: Gulf Professional Publishing; 2015. p. 149–234. https://doi.org/10.1016/B978-1-85617-830-3.00005-5.
[50] Yoo HM, Jeong S-Y, Choi S-W. Analysis of the rheological property and crystallization behavior of polylactic acid (Ingeo™ Biopolymer 4032D) at different process temperatures, vol. 21; 2021. p. 702–9. https://doi.org/10.1515/epoly-2021-0071. 1.
[51] Wang J, Yang B, Lin X, Gao L, Liu T, Lu Y, et al. Research of TPU materials for 3D printing aiming at non-pneumatic tires by FDM method. Polymers 2020. https://doi.org/10.3390/polym12112492.
[52] ASTM Standard D638. Standard test method for tensile properties of Plastics. West Conshohocken, PA: ASTM International; 2015. https://doi.org/10.1520/D0638-14.
[53] Dillard DA. Chapter 1 - fundamentals of stress transfer in bonded systems. In: Dillard DA, Pocius AV, Chaudhury M, editors. Adhesion science and engineering. Amsterdam: Elsevier Science B.V.; 2002. p. 1–44. https://doi.org/10.1016/B978-0-444-51140-9.50028-7.
[54] Chandra Shekar A, Hadj Djilani A, Zitoune R, Toubal L, Hof LA. Effect of input variables on the mechanical properties of additively manufactured PEEK thermoplastics. Mater Today Proc 2023. https://doi.org/10.1016/j.matpr.2023.09.101.
[55] Rodríguez-Reyna SL, Mata C, Díaz-Aguilera JH, Acevedo-Parra HR, Tapia F. Mechanical properties optimization for PLA, ABS and Nylon + CF manufactured by 3D FDM printing. Mater Today Commun 2022;33:104774. https://doi.org/10.1016/j.mtcomm.2022.104774.
[56] Gackowski BM, Goh GD, Sharma M, Idapalapati S. Additive manufacturing of nylon composites with embedded multi-material piezoresistive strain sensors for structural health monitoring. Compos B Eng 2023;261:110796. https://doi.org/10.1016/j.compositesb.2023.110796.
[57] Rahmatabadi D, Ghasemi I, Baniassadi M, Abrinia K, Baghani M. 3D printing of PLA-TPU with different component ratios: fracture toughness, mechanical properties, and morphology. J Mater Res Technol 2022;21:3970–81. https://doi.org/10.1016/j.jmrt.2022.11.024.
[58] Kumar Patro P, Kandregula S, Suhail Khan MN, Das S. Investigation of mechanical properties of 3D printed sandwich structures using PLA and ABS. Mater Today Proc 2023. https://doi.org/10.1016/j.matpr.2023.08.366.
[59] Marşavina Liviu, Vălean Cristina, Mărghitaș Mihai, Linul Emanoil, Razavi Nima, Berto Filippo, Brighenti Roberto. Effect of the manufacturing parameters on the tensile and fracture properties of FDM 3D-printed PLA specimens. Eng Fract Mech 2022;274:108766. https://doi.org/10.1016/j.engfracmech.2022.108766. ISSN 0013-7944.
[60] Vălean Cristina, Marşavina Liviu, Mărghitaș Mihai, Linul Emanoil, Razavi Nima, Berto Filippo. Effect of manufacturing parameters on tensile properties of FDM printed specimens. Procedia Struct Integr 2020;26:313–20. https://doi.org/10.1016/j.prostr.2020.06.040. ISSN 2452-216.
[61] Wang Qinglin, Zhang Gonghe, Zheng Xiaodong, Ni Yinxu, Liu Fenghua, Liu Yang, Xu Luoyu Roy. Efficient characterization on the interlayer shear strengths of 3D printing polymers. J Mater Res Technol 2023;22:2768–80. https://doi.org/10.1016/j.jmrt.2022.12.147. ISSN 2238-7854.
[62] Gonabadi H, Yadav A, Bull SJ. The effect of processing parameters on the mechanical characteristics of PLA produced by a 3D FFF printer. Int J Adv Des Manuf Technol 2020;111:695–709. https://doi.org/10.1007/s00170-020-06138-4.
[63] Anderson Isabelle. Mechanical properties of specimens 3D printed with virgin and recycled polylactic acid. 3D Print Addit Manuf 2017;4:110–5. https://doi.org/10.1089/3dp.2016.0054.